frontiers in Materials

ORIGINAL RESEARCH
published: 03 February 2022
doi: 10.3389/fmats.2021.796044

Optimizing Barium Titanate Nanocomposite Bone Scaffolds for Biomineralization in Dynamic Compression Bioreactors Using Time-Lapsed Microstructural Imaging and Smart Thresholding

*Gian Nutal Schädli[1,2], Helena David[2], Anke M. de Leeuw[1], Franklin Carlson[2], Lara Tenisch[1], Pascal Muff[1], Marina Rubert[1] and Ralph Müller[1]**

[1]Institute for Biomechanics, Department of Health Sciences and Technology, ETH Zurich, Zurich, Switzerland, [2]Particle Technology Laboratory, Department of Mechanical and Process Engineering, ETH Zurich, Zurich, Switzerland

OPEN ACCESS

Edited by:
Davide Ruffoni, University of Liège, Belgium

Reviewed by:
Aurélie Carlier, Maastricht University, Netherlands
Laoise Maria McNamara, National University of Ireland Galway, Ireland

***Correspondence:**
Ralph Müller
ram@ethz.ch

Specialty section:
This article was submitted to Mechanics of Materials, a section of the journal Frontiers in Materials

Received: *15 October 2021*
Accepted: *22 December 2021*
Published: *03 February 2022*

Citation:
Schädli GN, David H, de Leeuw AM, Carlson F, Tenisch L, Muff P, Rubert M and Müller R (2022) Optimizing Barium Titanate Nanocomposite Bone Scaffolds for Biomineralization in Dynamic Compression Bioreactors Using Time-Lapsed Microstructural Imaging and Smart Thresholding. Front. Mater. 8:796044. doi: 10.3389/fmats.2021.796044

Bone scaffolds made of calcium phosphate polymer nanocomposites have limited osteoinductive properties. Piezoelectric materials have attracted considerable interest in bone tissue engineering due to their potential to promote osteogenesis through additional electrical stimulation. Time-lapsed micro-CT imaging is a time-effective tool for *in vitro* optimization of such scaffolds but is challenged by nanocomposites with a high attenuation coefficient, such as one containing high amounts of piezoelectric barium titanate. We used high-resolution end-point micro-CT scans combined with histology and Raman spectroscopy to screen polydopamine functionalized nanocomposites containing 3–27 vol% barium titanate for collagenous extracellular matrix formation and mineralization. All compositions showed well-connected extracellular matrix and birefringent matured collagen after seven weeks of static human mesenchymal stem cell cultures. Nevertheless, high-resolution micro-CT analysis combined with smart thresholding during image processing enabled us to observe modest differences in ECM mineralization between groups suggesting that a volume fraction of 9–21% barium titanate facilitated the formation of dense mineral clusters in the pores even in the absence of mechanical stimuli, further corroborated by Raman spectroscopy. The same image processing approach facilitated the analysis of time-lapsed micro-CT images of scaffold cultures in dynamic compression bioreactors where 9 vol% barium titanate was the best nanocomposite composition, resulting in a significant twofold increased maturation rate under dynamic conditions. On the other hand, barium titanate content of ≥15 vol% did not improve mineralization. At 27 vol%, the biomineralization of the collagenous extracellular matrix was even impeded in the nanocomposite scaffolds, as evidenced by histology stainings. Overall, our approach enables time-lapsed quantitative assessment of high X-ray absorbing nanocomposite scaffolds for biomineralization under dynamic compression, facilitating the optimization of such mechanically responsive scaffolds.

Keywords: nanocomposite, barium titanate, bone scaffolds, dynamic compression bioreactors, time-lapsed

INTRODUCTION

Bone is a natural hierarchically structured composite composed of highly organized collagen bundles reinforced with hydroxyapatite nanocrystals. This tissue composition is piezoelectric and generates electrical charges under mechanical deformation (Khare et al., 2020). Bone possesses a natural healing capacity that is improved under cyclic loading and can repair cracks and small fractures (Malhotra et al., 2021) (**Figure 1A**). However, removing a bone tumor or traumatic injury can cause defects beyond a critical size (Schemitsch, 2017), requiring surgical intervention using fixation, bone autografts, or allografts. Such procedures are associated with increased risk and additional trauma for the patient, especially in aged individuals, thus, continue to drive materials design for bone scaffolds (Koons et al., 2020). Inspired by bone's piezoelectric properties, a growing body of literature uses such materials to improve the scaffold's efficacy for bone regeneration (Liu et al., 2020; Zhang et al., 2021).

Polymer nanocomposite materials are an increasingly attractive material choice for bone scaffolds because of their ability to outperform their individual constituents (Koons et al., 2020) (**Figure 1A**). Polymers such as poly (lactic-co-glycolic acid) (PLGA) are advantageous due to their tunable degradation time (Washington et al., 2017). The disadvantage of PLGA is its low wettability, cell adhesion (**Figure 1A**), and limited bioactivity, owing to the lack of functional groups for protein adsorption or cell adhesion (Gentile et al., 2014). An attractive and facile technique to functionalize hydrophobic polymers is polydopamine coating, which was inspired by the mussels' ability to adhere to almost any surface (Lee et al., 2007). Barium titanate has attracted much attention for enhancing the polymer's and scaffold's osteoinductive properties owing to its biocompatibility and piezoelectricity properties (Khare et al., 2020; Liu et al., 2020). Such composite scaffolds were produced with a wide range of barium titanate content (Khare et al., 2020), but the scaffolds were seldomly tested under controlled cyclic loading. We have previously shown that nanocomposite scaffolds with a 3:7 volume ratio between barium titanate and hydroxyapatite enhanced bone formation during longitudinal *in vitro* experiments in dynamic compression bioreactors compared to the widely used pure hydroxyapatite

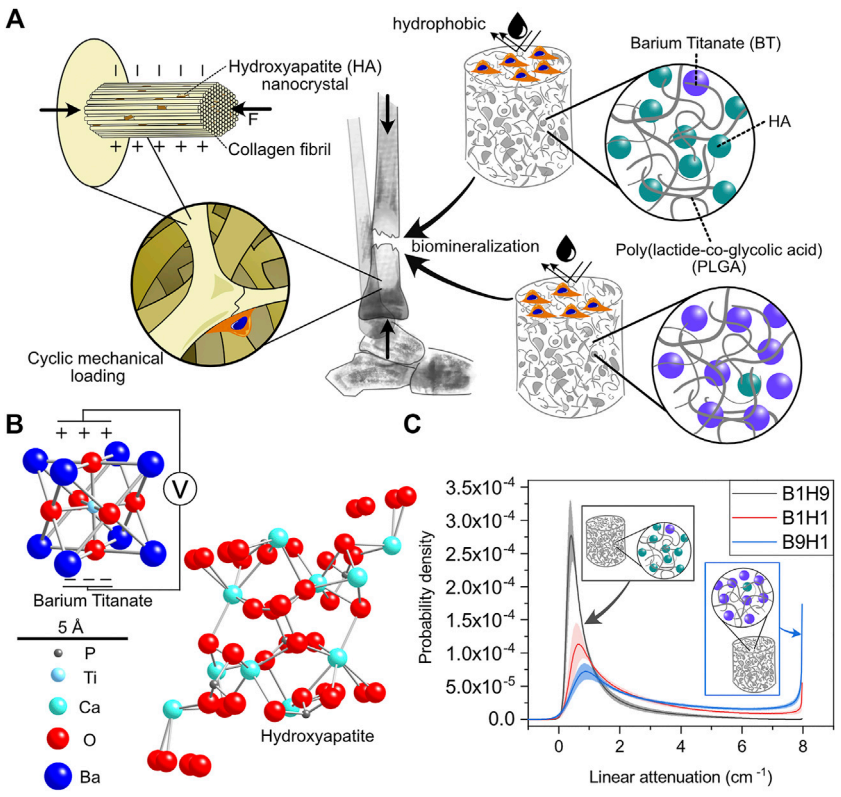

FIGURE 1 | Challenges in nanocomposite development for bone scaffolds. **(A)** Schematic illustration of the natural nanocomposite bone and nanocomposite scaffolds for bone tissue engineering with various barium titanate and hydroxyapatite compositions. **(B)** Unit cells of barium titanate and hydroxyapatite. **(C)** Histograms of linear attenuation coefficients obtained from high-resolution micro-CT of scaffolds containing barium titanate and hydroxyapatite in a volume ratio of 1:9 (B1H9), 1:1 (B1H1), or 9:1 (B9H1). The line represents the mean and the shaded area the s.d.

nanocomposite scaffolds (Schädli et al., 2021). Yet, there remain contrasting results about the barium titanate content that promotes osteogenesis and mineralization in polymer nanocomposite or ceramic composite scaffolds.

A 42.6 vol% barium titanate in polymer nanocomposite scaffolds was considered ideal for promoting osteoblast growth (Tang et al., 2021). In aligned porous barium titanate/hydroxyapatite ceramic composites, 70 vol% barium titanate showed the best cell viability; solid ceramic composites with approximately 80 vol% had the highest early osteogenic activity under cyclic loading (Tang et al., 2017). On the other hand, 5–10 vol% barium titanate in polymer nanocomposite membranes was shown to enhance bone regeneration (Lopes et al., 2013; Zhang et al., 2016). Thus, a systematic investigation of different barium titanate concentrations in 3D porous polymer nanocomposite scaffolds cultured under cyclic loading is required to find compositions that promote biomineralization (**Figure 1A**). However, the high X-ray absorption of barium titanate poses a challenge to standard image processing of micro-CT scans that mostly evolved around imaging bone-like materials such as hydroxyapatite. This challenge is because the unit cell of barium titanate is smaller than hydroxyapatite. At the same time, the element barium has a higher atomic Z number than phosphorus (**Figure 1B**), giving barium titanate twice as high density as hydroxyapatite. Therefore, the linear attenuation distribution of such polymer nanocomposite scaffolds widens with increasing vol% content of barium titanate (**Figure 1C**), making it more difficult to detect biomineralization due to lower attenuation properties of hydroxyapatite. Furthermore, artifacts (partial volume effects and beam hardening) might occur at the scaffold border (Li et al., 2015), requiring refined image processing methods to distinguish newly formed minerals from the existing scaffold material. *In vivo*, such challenges were overcome by longitudinally monitoring the bone and implant using time-lapsed micro-CT (Li et al., 2015).

In this study, we first established a surface functionalization to render the polymer nanocomposite scaffolds hydrophilic. The surface functionalization method was based on self-oxidizing polydopamine coating. Then, we cultured human mesenchymal stem cells (hMSCs) on functionalized nanocomposite scaffolds containing various barium titanate to hydroxyapatite ratios to investigate the influence of barium titanate content on *in vitro* biomineralization. We studied this material's effect on extracellular matrix formation and mineralization during 7 weeks of *in vitro* cell culture without mechanical stimuli and in dynamic compression bioreactors. High-resolution end-point micro-CT scans were combined with histology and Raman spectroscopy to elucidate collagenous extracellular matrix formation and mineralization. Finally, dynamic compression bioreactors and time-lapsed imaging, combined with smart thresholding, were used to reveal large differences between scaffolds containing a small to large vol% of barium titanate nanoparticles, highlighting the importance of assessing such materials under controlled cyclic loading.

TABLE 1 | The volume ratio of barium titanate (BT) to hydroxyapatite (HA) and barium titanate filler content.

Name	BT:HA vol. Ratio	BT filler content (vol%)
B1H9	1:9	3
B3H7	3:7	9
B1H1	1:1	15
B7H3	7:3	21
B9H1	9:1	27

RESULTS

Screening Different Nanocomposite Scaffold Compositions Under Static Cell Culture Conditions

The hydrophilicity and cell adhesion of hydrophobic barium titanate polymer nanocomposite scaffolds were improved by systematically investigating the effect of polydopamine surface functionalization on the water contact angle (**Supplementary Figure S1**). Afterward, the bioactivity of polymer nanocomposite scaffolds containing mixtures of barium titanate and hydroxyapatite nanoparticles with volume ratios from 1:9 to 9:1, corresponding to 3–27 vol% of barium titanate, was tested under static cell culture conditions. We refer to these nanocomposites with the following group names: B1H9, B3H7, B1H1, B7H3, B9H1, where the numbers reflect the volume ratio and the letter stands for the material, i.e., B for barium titanate and H for hydroxyapatite. **Table 1** summarizes all nanocomposites that were produced and characterized for this study. After 1 week of culture, hematoxylin and eosin staining showed a well-connected extracellular matrix with a spread cell morphology in all scaffold compositions (**Figures 2A–C**). The cells penetrated the scaffolds and adhered to the scaffold surface. However, the scaffold's core remained mostly cell-free (**Supplementary Figure S2A**). Von Kossa staining of sequential sections was brownish and showed a similar morphology to the hematoxylin and eosin staining, indicating the early stage of amorphous calcium phosphate mineralization in matrix vesicles (Boonrungsiman et al., 2012; Hasegawa, 2018). The extracellular matrix was denser after 7 weeks of cell culture (**Figures 2D–F**, **Supplementary Figure S2B**). The von Kossa staining revealed densely formed black mineral nodules. In the B1H1 nanocomposite scaffold, large (50 μm) mineral clusters were observed.

The von Kossa method also stained the nanocomposite scaffold. We, therefore, used Raman spectroscopy to identify the composition of the formed mineral unambiguously. **Figures 2G–I** show micrographs of the different scaffold compositions, and **Figure 2J** depicts the corresponding spectra from the spots highlighted in the micrographs by circles. Spectra obtained within the scaffold showed the vibration bands of barium titanate (Schädli et al., 2017) at 307, 457, and 717 cm^{-1}, the characteristic vibration band of PLGA at

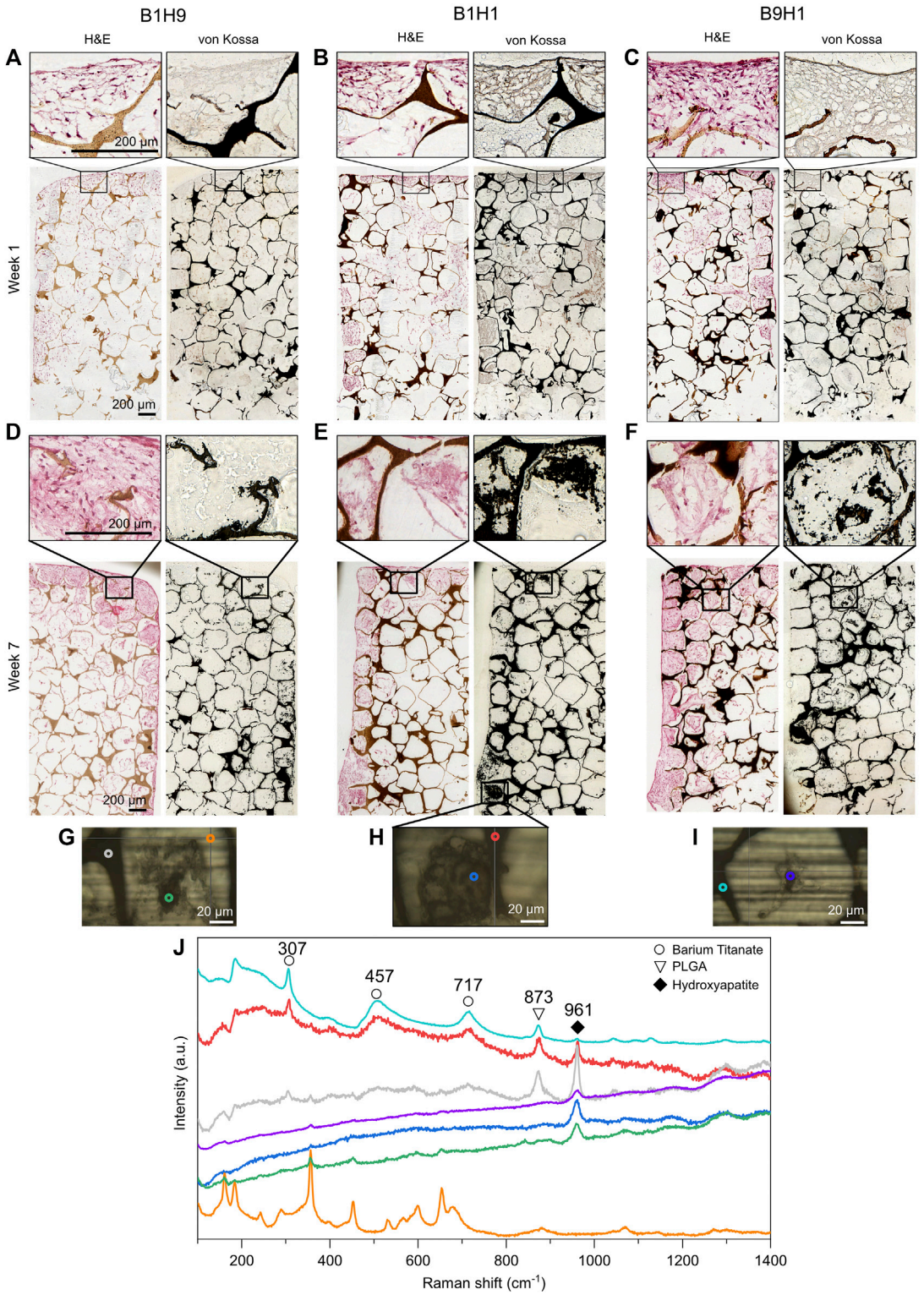

FIGURE 2 | Static cell culture of nanocomposite scaffolds. **(A-C)** Hematoxylin and eosin staining (H&E) and von Kossa staining of B1H9, B1H1, and B9H1 nanocomposite scaffolds after 1 week and **(D-F)** 7 weeks. **(G-I)** Micrographs of the location of Raman spectra measurements and **(J)** the corresponding Raman spectra; the colors of the spectra correspond to the different regions in **(G–I)**. The circle indicates vibration bands from barium titanate, the triangle marks the characteristic vibration band of the polymer PLGA, and the diamond highlights the characteristic peak of hydroxyapatite. The orange spectrum taken in the background corresponds to the Kawamoto tape used for sectioning. N = 2 samples were sectioned for each group.

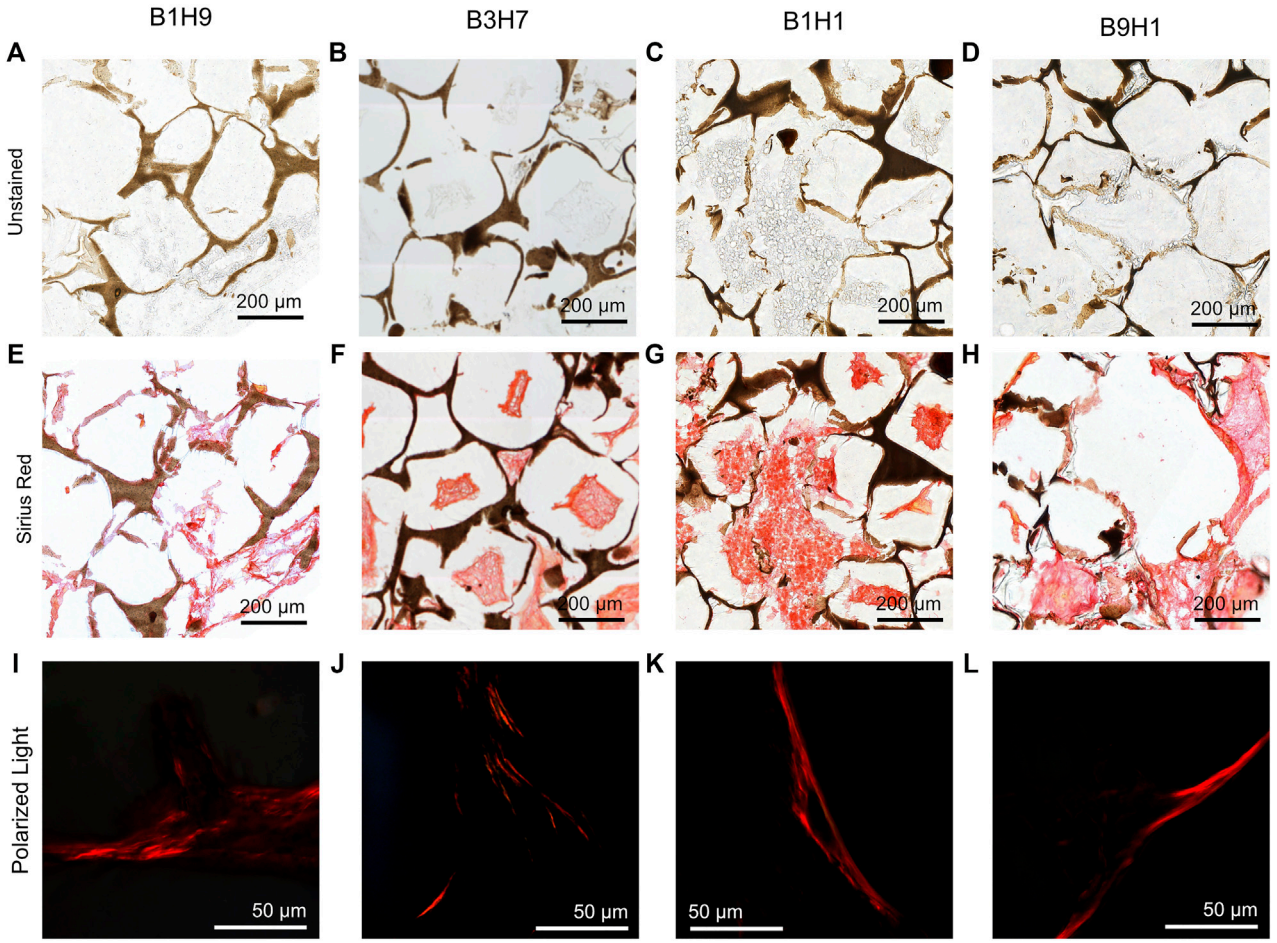

FIGURE 3 | Collagenous extracellular matrix formation. **(A)** Microscopy images of unstained B1H9, **(B)** of B3H7, **(C)** of B1H1, and **(D)** of B9H1 nanocomposite scaffolds; **(E-H)** the same samples stained with Picro Sirius Red. **(I-L)** Representative polarized light microscopy images of birefringent collagen fibers in the nanocomposite scaffolds. Horizontal scaffold sections were taken from the top 300 µm of the scaffolds. N = 2 samples were sectioned for each group.

875 cm^{-1} and the characteristic PO_4^{3-} stretching vibration of hydroxyapatite (Khalid et al., 2018) at approximately 961 cm^{-1}. The relative peak intensity of the constituents corresponded to the scaffolds' composition. Raman spectra obtained within mineral clusters in the pores showed the PO_4^{3-} stretching vibration only, confirming the cell-mediated mineral formation of the observed structures. The cell-made mineral formation was also corroborated by significantly ($p < 0.05$) elevated alkaline phosphatase activity at Days 7 and 14 (**Supplementary Figure S3**).

Bone is composed of minerals and collagen. We, therefore, investigated next in four different compositions of varying barium titanate to hydroxyapatite volume ratios if the cells also secreted collagen (**Figure 3**). Unstained histology cross-sections showed the formation of large mineral clusters in the pores of B1H1 nanocomposites (**Figure 3C**). These mineral clusters coincided with the collagenous extracellular matrix (ECM), visualized by Picro Sirius Red, proving cell-mediated mineral formation. In B1H9 (**Figure 3A**), B3H7 (**Figure 3B**), and B9H1 (**Figure 3D**) scaffolds, the mineral nodules did not form big clusters. The collagenous ECM (**Figures 3E–H**) exhibited birefringence in all nanocomposites (**Figure 3I–L**). Furthermore, confocal microscopic images (**Figures 4A–D**) showed osteocalcin within the formed ECM (**Figures 4E–H**). The formed mineral in these scaffolds was also detected in registered micro-CT scans but was limited in resolution and accuracy using standard image processing methods (Schulte et al., 2011) because of the high absorption properties of barium titanate (**Supplementary Figure S4**).

Figure 5 shows the quantitative analysis of the high-resolution micro-CT scans using dilations during image processing. The pores of the scaffolds were defined as the volume of interest. For each sample, an individual threshold was calculated based on the linear attenuation distribution (**Figure 1C**) to determine the scaffold geometry that was then dilated to reduce partial volume effects (Li et al., 2015). In B1H1 scaffolds, many large mineral clusters were formed

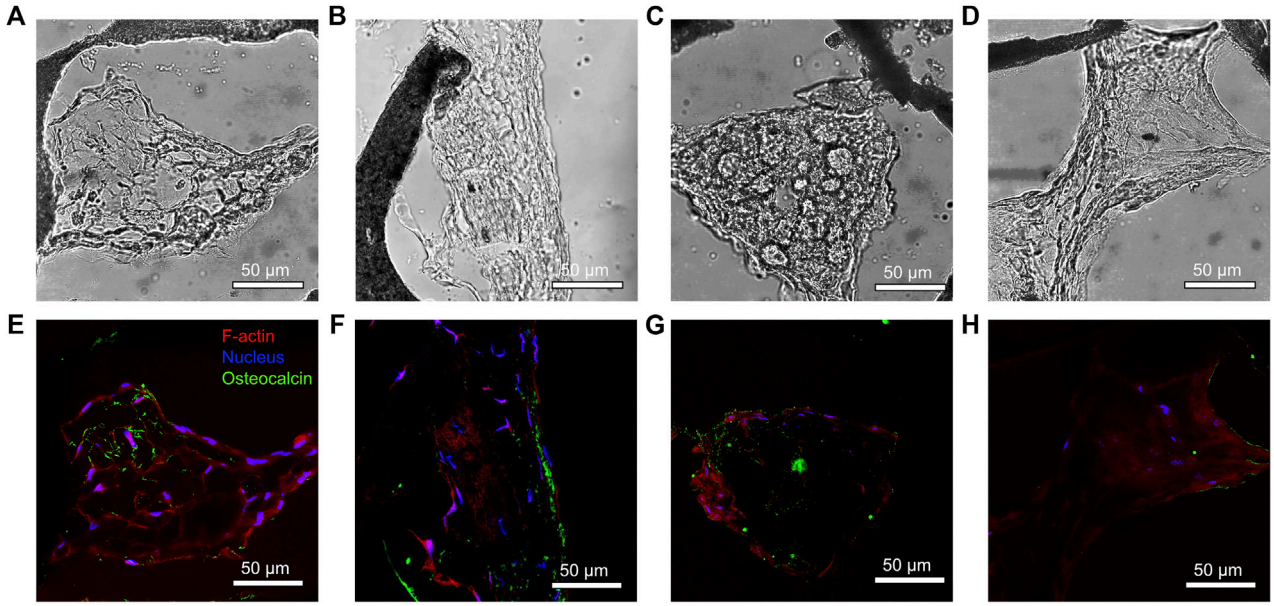

FIGURE 4 | Osteogenic differentiation of stem cells. **(A-D)** Brightfield laser scanning confocal microscopy images of **(A)** B1H9, **(B)** B3H7, **(C)** B1H1, and **(D)** B9H1 sections. **(E-H)** Corresponding images of osteocalcin immunostaining. Horizontal scaffold sections were taken from the top 300 µm of the scaffolds. N = 2 samples were sectioned for each group.

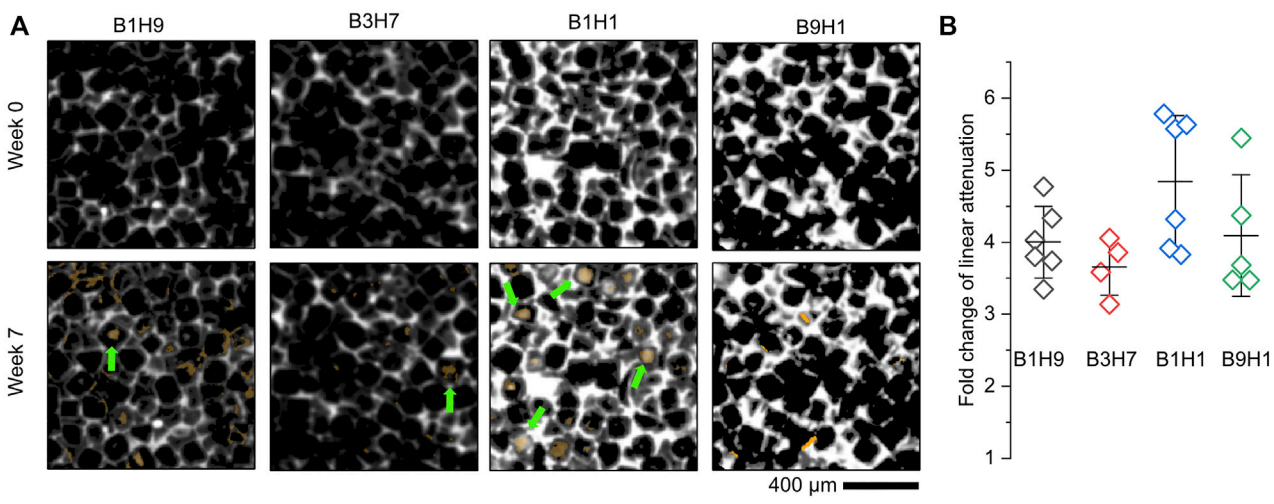

FIGURE 5 | High-resolution micro-CT analysis after 7 weeks of static culture. **(A)** Grayscale micro-CT images of B1H9, B3H7, B1H1, and B9H1 nanocomposite scaffolds before and after the cell culture. The formed mineral is highlighted in orange. The yellow arrows point to mineral clusters in the pores. The scaffolds appear brighter with an increase in barium titanate content within the composition. **(B)** Fold change of the linear attenuation within the pores of these scaffolds before and after culture; B1H9 (n = 6), B3H7 (n = 4), B1H1 (n = 6), and B9H1 (n = 5) samples. The data are shown as mean ± s.d. A statistically significant difference was tested by one-way ANOVA with Holm-Bonferroni post-hoc correction. No significant difference was found.

inside the pores, while in B1H9 scaffolds, the mineral formation was also detected around the scaffold structure (**Figure 4A**). We analyzed the fold change in linear attenuation caused by the mineral formation between the two time-points (**Figure 4B**) because the images had different attenuation baseline values, which was also observed by the increase in image brightness with the amount of embedded barium titanate in the polymer

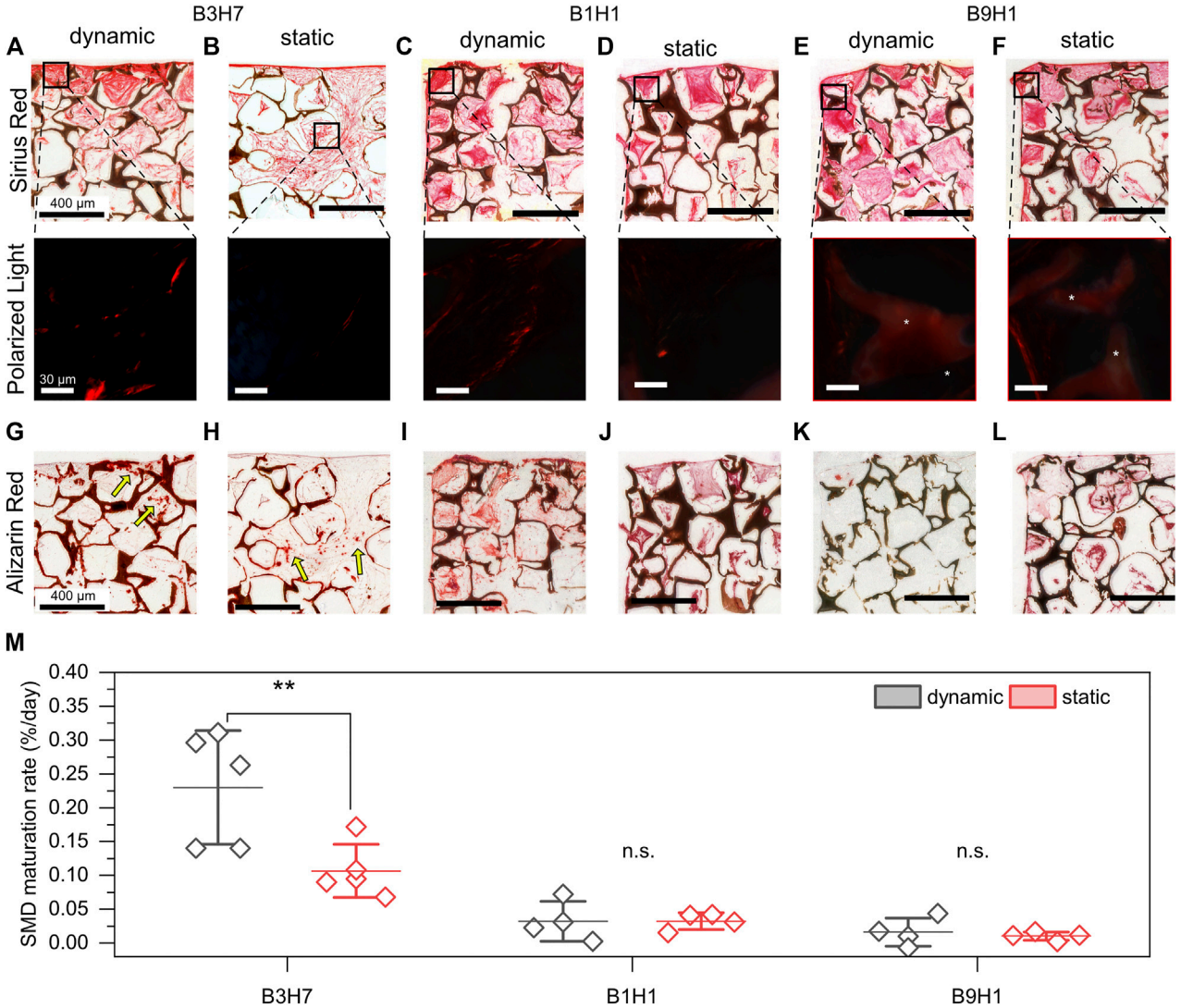

FIGURE 6 | Extracellular matrix mineralization after 7 weeks in dynamic compression bioreactors. **(A-F)** Vertical cross-sections stained with Picro Sirius Red of B3H7, B1H1, and B9H1 nanocomposite scaffolds under static **(B,D,F)** or dynamic **(A,C,E)** conditions. The magnifications show a birefringent collagenous matrix imaged with polarized light microscopy. The white asterisk indicates the scaffold. **(G-L)** Sequential cross-sections of the same nanocomposite scaffolds stained with Alizarin Red. N = 2 samples were processed for the stainings. **(M)** Scaffold mineral density maturation rate was monitored by time-lapsed micro-CT imaging of B3H7 (n = 5), B1H1 (n = 4) scaffolds, and B9H1 (n = 4) scaffolds. A statistically significant difference was tested by a two-way repeated measurements ANOVA with Holm-Bonferroni post-hoc correction, $^{**}p < 0.01$, n.s. no significant change. The B3H7 rates are from Schädli et al., 2021.

nanocomposite. Although not significant, B1H1 scaffolds showed an elevated fold change compared to the other compositions.

Longitudinal *in vitro* Cell Culture in Dynamic Compression Bioreactors

Finally, we investigated the B1H1 and B9H1 nanocomposites during a 7-week *in vitro* cell culture in dynamic compression bioreactors that enable the culture of two scaffolds per bioreactor (Schädli et al., 2021) and compared the results to our previous work (Schädli et al., 2021). One scaffold was exposed to cyclic loading for 5 min three times per week, while the other was cultured under static conditions (Schädli et al., 2021). The scaffolds were loaded at 5 Hz, which is within physiological loading as, during running, the impact shock frequency generated from heel strike is typically within 3–20 Hz (Gruber et al., 2014). Furthermore, mechanical loading with 5 Hz was shown to result *in vivo* in increased bone net remodeling rates (Scheuren et al., 2020). Histology sections were stained with Picro Sirius Red and Alizarin Red after 1 week of culture (**Supplementary Figure S5**) to determine the maturation of the mineralized matrix. In both B1H1 and B9H1 scaffold compositions, the Picro Sirius Red stain revealed abundant collagenous ECM already after 1 week. However, this collagenous ECM did not yet exhibit birefringence

(**Supplementary Figure S5A–B**). The Alizarin Red stain was faint, indicating low mineralization of the ECM (**Supplementary Figure S5C–D**).

After 7 weeks of culture in dynamic compression bioreactors, the Picro Sirius Red staining was more intense (**Figures 6A–F**). Under dynamic conditions, the ECM was more distributed (**Figures 6A,C,E**) within the pores than under static conditions (**Figures 6B,D,F**). The collagenous ECM matured during culture and exhibited birefringence in all nanocomposite scaffolds (**Figures 6A–F**) under polarized light microscopy, indicating thicker collagen fibrils (Bromage et al., 2003). The B3H7 and B1H1 nanocomposite scaffold cultured under dynamic conditions showed the most considerable amount of birefringent collagen (**Figures 6A,C**). Interestingly, in B9H1 nanocomposite scaffolds cultured under dynamic conditions (**Figure 6E**), there was less birefringent collagen than under static conditions (**Figure 6F**). Also, the Alizarin Red staining was more intense after 7 weeks of culture in dynamic compression bioreactors (**Figure 6G–L**). The observed morphology of the stained mineralized ECM was in agreement with the stained collagenous ECM (**Figures 6A–F**), suggesting collagen mineralization (Hasegawa, 2018). In B3H7 and B1H1 scaffolds, the collagenous ECM mineralized under static and dynamic conditions (**Figures 6G–J**). Surprisingly, in B9H1 scaffolds, mineralization occurred only under static conditions (**Figure 6L**), while under dynamic conditions, no distinct mineralization was found (**Figure 6K**).

Time-lapsed micro-CT imaging during the culture allows monitoring of the ongoing ECM mineralization (Hagenmüller et al., 2007; Schädli et al., 2017). The scaffolds exhibited high apparent (>800 mg HA/cm^3) mineral densities (**Supplementary Figure S6A–B**) due to their high X-ray attenuation properties. Therefore, these regions were masked by a second upper threshold (**Supplementary Figure S6C**) to reduce changes in the measured mineral densities due to changes in the scaffold structure. Additionally, the scaffold was evaluated in the top region (**Supplementary Figure 7A–B**) due to the cell distribution. Finally, we calculated the maturation rate by linear fits to the scaffold mineral density maturation values (**Supplementary Figure S7C**) and compared it to our previous work (Schädli et al., 2021) (Figure 6M). Scaffolds with 9 vol% barium titanate (B3H7) had a 30 times higher maturation rate under static conditions than with 15 vol% barium titanate (B1H). In B3H7 scaffolds, the maturation rate was significantly higher under dynamic conditions and significantly higher than pure hydroxyapatite polymer nanocomposite scaffolds (Schädli et al., 2021). Dynamic conditions did not result anymore in higher scaffold mineral density maturation rates in B1H1 and B9H1 scaffolds. The measured maturation rate decreased almost by 50% when the barium titanate content was increased from 15 to 27 vol%. The result was validated by comparing the maturation rate values of the top region to the scaffold's bottom core, which was mainly cell-free (**Supplementary Figure 7D–I**).

DISCUSSION

A surface functionalization for polymer nanocomposite bone scaffolds by polydopamine coating and RGD was established in this study (**Supplementary Figure S1**). The scaffolds incorporated 3 to 27 vol% barium titanate by varying the barium titanate to hydroxyapatite volume ratio. Barium titanate is a biocompatible piezoelectric ceramic (Khare et al., 2020). The surface charges of piezoelectric biomaterials are associated with improved cell proliferation and osteogenesis (Damaraju et al., 2017; Ehterami et al., 2018; Zhang et al., 2018, 2021; Kitsara et al., 2019; Liu et al., 2020). On the other hand, the large attenuation coefficient of barium titanate introduces challenges in mineral analysis by micro-CT. We seeded the scaffolds with hMSCs and cultured them under static cell culture conditions with end-point high-resolution micro-CT scans and subsequently in dynamic compression bioreactors. During cell culture in dynamic compression bioreactors, the scaffold mineralization was monitored by time-lapsed micro-CT imaging (Schädli et al., 2021). The focus of this study was to optimize the barium titanate vol% in polymer nanocomposite for promoting hMSC extracellular matrix mineralization under cyclic loading, emulating *in vivo* conditions.

Surface functionalization of 2D nanocomposite films (**Supplementary Figure S1A-C**) was easily established by polydopamine coating, in line with previous studies (Chien and Tsai, 2013; Firoozi and Kang, 2020). However, large 3D porous hydrophobic polymer nanocomposite scaffolds required an intermediate PVA coating during fabrication to enable a functionalization by polydopamine and RGD (**Supplementary Figure S1**). This surface functionalization successfully improved the wettability of the scaffolds and increased cell spreading. Under static cell culture conditions, the B1H1 nanocomposite scaffolds, containing 15 vol% barium titanate, modulated the mineral formation toward large clusters, located in the scaffold's pore space. We identified these mineral clusters unambiguously as hydroxyapatite by Raman spectroscopy (**Figure 2J**) and showed that their origin was osteoblastic extracellular collagenous matrix mineralization (**Figures 3** and **4**). Furthermore, the mineral clusters in B1H1 nanocomposite were denser, as shown by image registration of end-point high-resolution micro-CT scans of the scaffolds combined with smart thresholding focusing on the pore volume (**Figure 5**). The mineral formation inside the void spaces supports the proposed mechanism for material-induced heterotropic ossification (Bohner and Miron, 2019). The most striking differences between the different scaffold compositions were found under dynamic conditions (**Figure 6**).

In B1H1 nanocomposite scaffolds cultured under dynamic conditions, collagen matured more homogenously within the ECM. Also, time-lapsed micro-CT imaging showed a significant increase in scaffold mineral density. Surprisingly, the B9H1 scaffolds, having 27 vol% of barium titanate, showed no mineralization of the collagenous ECM when cultured under dynamic conditions (**Figure 6K**). During the cell culture, time-lapsed micro-CT imaging did not detect a significant change in the B9H1 scaffolds. Time-lapsed micro-CT imaging allows obtaining several scans from the same scaffold over time. Thus, even mineralization that only contributed to a relatively small change (few %) in mineral density becomes detectable despite to the high absorbing scaffold material. The scaffold

mineral density maturation rate obtained only through time-lapsed micro-CT showed that the optimal barium titanate concentration in these polymer nanocomposite scaffolds was in the range of 9–15 vol% (Figure 6M) while higher concentrations even impeded ECM mineralization under dynamic conditions (**Figure 6K**).

Composite biomaterials are an increasingly attractive choice for bone scaffolds because of their ability to outperform their constituents (Koons et al., 2020). The polymer PLGA is often used as a polymer matrix because of its tunable degradation time (Gentile et al., 2014). However, PLGA lacks functional surface groups for protein adsorption or cell adhesion (Gentile et al., 2014). Polydopamine-assisted functionalization of 3D porous PLGA scaffolds with an osteoinductive peptide were previously shown (Ko et al., 2013). However, these PLGA scaffolds were only 1 mm thin, while the scaffolds were 3 mm thick in this study. It was not feasible to functionalize the thick, cylindrical scaffolds using a polydopamine approach as the coating solution could not penetrate the microporous hydrophobic scaffold.

Critical-sized long bone defects typically require long, cylindrically shaped scaffolds (Pobloth et al., 2018). We showed a facile implementation for polydopamine surface functionalization via an intermediate PVA coating introduced during salt leaching. It was shown that PVA adsorbs well on hydrophobic substrates (Kozlov et al., 2003) and renders them hydrophilic. Hydrophilicity alone did not greatly improve cell spreading but enabled the surface functionalization of large, initially hydrophobic 3D microporous nanocomposite scaffolds via polydopamine and RGD. This surface functionalization resulted in well-spread hMSCs already after 1 day (**Supplementary Figure S1D**), similar to another study where fibroblasts were seeded on zirconia substrates (Yang et al., 2020). In addition, we showed that the barium titanate vol% content modulated cell-mediated mineral formation in the nanocomposite scaffolds (**Supplementary Figure S4**). Tang et al., 2017 showed that osteoblasts exhibited higher ALP activity when cultured on bioceramics with 90 wt% barium titanate and 10 wt% hydroxyapatite than on pure ceramics but only when the bioceramic was cyclically loaded. However, they did not investigate if the increased ALP activity also resulted in elevated mineralization or ECM formation.

Osteoblasts secrete the non-mineralized matrix material osteoid that is mainly composed of type I collagen and other proteins such as osteocalcin. Afterward, the osteoid mineralizes through vesicular and fibrillar phases (Florencio-Silva et al., 2015). During these phases, the enzyme ALP is required to hydrolyze organic phosphate but is insufficient to assess the scaffold's efficacy for mineral formation. In this study, the ALP activity was significantly increased in intermediate time-points before it decreased again to low values at the end (**Supplementary Figure S3**), in agreement with other works that assessed ALP activity in long cell cultures (Koroleva et al., 2015). Analysis of high-resolution micro-CT indicated that the B1H1 scaffolds (15 vol% barium titanate) promoted the mineral formation of dense mineral clusters in the pores, but overall, the differences between the scaffolds remained small under the static cell culture conditions (**Figure 5**).

In a previous study, we showed that nanocomposite scaffolds containing a barium titanate and hydroxyapatite mixture with a 3:7 vol. ratio, having 9 vol% barium titanate, exhibited a five times higher mineral maturation rate than scaffolds containing only hydroxyapatite (Schädli et al., 2021). Furthermore, we observed significantly increased bone formation under dynamic conditions compared to static culture conditions. However, even though B1H1 nanocomposite scaffolds exhibited more matured collagenous ECM under dynamic conditions (**Figures 6C,D**), the mineralization was not enhanced compared to static conditions (**Figures 6I,J,M**). Most notably, cyclic loading of the B9H1 nanocomposite scaffolds impeded the mineralization of the collagenous ECM (**Figure 6K**). The comparison to our previous work (Schädli et al., 2021) showed that cyclic loading, induced by the dynamic compression bioreactors, was instrumental in determining an optimal concentration in the range of 9–15 vol% that facilitates ECM mineralization (Figure 6M). A potential mechanism could be the scaffolds' piezoelectric properties which depend on the barium titanate filler vol% (Zhang et al., 2014). We expect that the reported effects (scaffold mineral density maturation rate, abundance of extracellular matrix) depend on the cell seeding density but that the differences between the dynamic and static samples within the same group are independent of the cell seeding density.

Composite membranes composed of P(VDF-TrFE) as matrix and 5 vol% barium titanate nanoparticles had a surface potential of -76.6 mV within the endogenous range (-60 to -100 mV) and showed improved bone formation *in vivo* (Zhang et al., 2016). However, in a follow-up study (Zhang et al., 2018), membranes with a surface potential of -53 mV exhibited improved osteogenic properties compared to those with -78 mV. Titanium alloys coated with polarized barium titanate nanoparticles had a surface potential of -30 mV and promoted bone formation *in vivo* by increasing intracellular Ca^{2+} concentration (Liu et al., 2020). Mineralization of collagenous ECM was enhanced on electrospun PVDF fiber scaffolds with -95 mV surface potential compared to -173 mV. An increase in barium titanate content can be associated with higher piezoelectric properties (Ehterami et al., 2018); thus, it is possible that under cyclic loading, the B1H1 and B9H1 nanocomposite scaffolds created an electrical microenvironment that interferes with the endogenous electric fields produced by membrane potentials. Previously, it was shown that depolarization of the cell's membrane potential suppresses osteogenic differentiation of hMSCs (Sundelacruz et al., 2019). In fact, attempts have been made to stimulate bone regeneration by activating the PI3K-AKT signaling pathway through the production of physiologically relevant electric signals (Kapat et al., 2020). Future work should therefore focus on associating the piezoelectric properties of the scaffold with the biomineralization under various loading regimes for a better understanding of the role of electrical stimulus in biomineralization. Such experiments could potentially also explain the 50% decrease in mineral density maturation between B1H1 and B9H1 scaffolds when the nanoparticle content was increased from 15 to 27 vol%

(**Figure 6M**), as previous work has shown a linear relationship between piezoelectric property and barium titanate content (Ehterami et al., 2018).

Previous studies have used piezoresponse force microscopy, Kelvin probe force microscopy, or surface ζ-potential measurements to determine the electric properties of nanocomposite scaffolds (Zhang et al., 2016, 2018; Szewczyk et al., 2019; Liu et al., 2020). However, these methods are designed to assess the surface property of the material. While the results provide insights into the interaction of cells directly adhering to the surface, they might not reflect the microenvironment of cells located in the void space of the microporous scaffolds presented in this work, even more so when the scaffold is cyclically loaded. Unfortunately, measurements of the overall piezoelectric properties, such as in a parallel plate configuration (Damaraju et al., 2017), were not feasible because the scaffold's porosity and stiffness did not provide a good interface to establish contact with an electrode. Despite that, we could assume that an increase in barium titanate content has increased the piezoelectric properties, as previously shown (Zhang et al., 2014). In the future, we suggest that such properties should be studied in geometries having a homogeneous and controlled morphology.

A growing number of reports found a relationship between electrical stimuli and activation of voltage-gated Ca^{2+} ion channels (Kapat et al., 2020; Camarero-Espinosa and Moroni, 2021). These channels regulate calcium influx into the cell (Camarero-Espinosa and Moroni, 2021). Hence, analysis of intracellular Ca^{2+} ion concentration (Liu et al., 2020) and ion channel-related gene expression (Camarero-Espinosa and Moroni, 2021) would be instrumental in improving our understanding of ECM mineralization in these nanocomposite scaffolds.

A further limitation was the high linear attenuation of the scaffolds containing a large (27 vol%) amount of barium titanate, e.g., B9H1 nanocomposite scaffolds. In addition, the high density of barium titanate (6.02 g/cm^3) led to beam hardening and increased partial volume effects. Therefore, voxels close to the scaffold have an artificially high gray value (Li et al., 2015). As the scaffold pore geometry was highly irregular, we used individual thresholds for each scaffold composition combined with a binary dilation operation to mask the scaffold (Li et al., 2015). This approach worked well with end-point high-resolution micro-CT scans to differentiate formed minerals from the scaffold. However, in the longitudinal experiment, the mineralization in B9H1 scaffolds cultured under static conditions was barely detectable due to the lower resolution of the micro-CT scans. This limitation was magnified by the highly irregular scaffold geometry (varying scaffold wall thickness and shapes) that resulted from the salt leaching production. Nevertheless, time-lapsed microstructural imaging to monitor scaffold biomineralization in dynamic compression reactors remains a sensitive tool as it aggregates multiple measurement points for a single sample compared to end-point biochemical methods. The production of nanocomposite scaffolds with regular morphology, as readily achieved through 3D printing (Schipani et al., 2020), would further facilitate the analysis by applying the presented smart thresholding approach, further reducing the limitations caused by a high percent content of barium titanate.

In conclusion, we have shown that hydrophobic microporous nanocomposite scaffolds are easily functionalized by polydopamine via an intermediate PVA coating. The hMSCs seeded on these functionalized scaffolds secreted abundant collagenous ECM. Under static conditions, the differences in ECM mineralization were modest, despite the large changes in barium titanate nanofiller content from 3 to 27 vol% that were accurately reflected by Raman spectroscopy analysis. Nevertheless, high-resolution micro-CT analysis and histology results suggested that the barium titanate filler content modulated the collagenous ECM mineralization in the absence of mechanical stimulation. Despite the strongly X-ray absorbing properties of scaffolds containing large fractions of barium titanate, this observation could be made thanks to smart thresholding to mask the scaffold geometry, focusing the mineral analysis on the pores. The same image processing approach facilitated the analysis of time-lapsed micro-CT images of scaffolds cultures in dynamic compression bioreactors. We showed by time-lapsed micro-CT analysis and end-point histology that mineralization of collagenous extracellular matrix was impeded in scaffolds containing a large amount of barium titanate when cultured under cyclic loading in dynamic compression bioreactors. To the best of our knowledge, nanocomposite scaffolds incorporating a wide variation of barium titanate nanoparticles have so far not been quantitatively assessed under controlled dynamic compression. Our approach enables time-lapsed quantitative assessment of high X-ray absorbing nanocomposite scaffolds for biomineralization under dynamic compression, facilitating the optimization of such mechanically responsive scaffolds in light of potential future applications in load-bearing bones.

MATERIALS AND METHODS

Nanocomposite Scaffold Preparation

Both nanoparticle powders, hydroxyapatite with an average particle diameter of 100 nm (677418, Sigma-Aldrich) and barium titanate (467634, Sigma-Aldrich, Merck & Cie, Schaffhausen, Switzerland) with 60 nm, were of spherical shape (Schädli et al., 2021). Nanocomposite scaffolds containing barium titanate and hydroxyapatite mixtures with a 9:1, 7:3, 1:1, 3:7, 1:9 volume ratio or pure hydroxyapatite were prepared following a modified solvent casting particulate leaching method (Schädli et al., 2021). First, barium titanate and hydroxyapatite nanoparticles were dispersed in chloroform (C2432, Sigma-Aldrich, Merck & Cie, Schaffhausen, Switzerland) by ultrasonication (SONICS®, Newton, CT, USA). Afterward, the polymer PLGA (Resomer® LG 855 S, Evonik, Essen Germany) was added. The total nanoparticle content in the polymer was held constant at approximately 30 vol%. The mixture was homogenized in a dual asymmetric centrifuge (Camenzind et al., 2010) (FlackTek SpeedMixer™ 150 FVZ, Hauschild Engineering, Hamm, Germany) at 3,000 rpm until all the polymer granules dissolved (6 × 5 min intervals), forming a nanocomposite slurry. Then, NaCl microparticles (250–315 µm)

were added as porogen in a 12:1 wt. ratio to the polymer to obtain a porosity above 80% (Schädli et al., 2021). After that, the compound was mixed in the SpeedMixer™ in 2-min intervals to allow excess solvent evaporation until the compound became smooth and moldable. Finally, the compound was pressured molded with 0.5 MPa (tecsis, F1119/P3962, Wika Schweiz, Hitzkirch, Switzerland) into cylindrical ferritic nitrocarburized steel molds of 40 mm height, 6 mm inner diameter (X153CrMoV12, Thyssenkrupp, Esse, Switzerland), and dried overnight at ambient conditions. The next day, the raw scaffold bars were removed from the mold, dried for another night at ambient conditions, and then for 24 h in a vacuum desiccator (<0.2 mbar). The dried raw scaffold bars were cut (Isomet low speed saw, Buehler, Leinfelden-Echterdingen, Germany) into cylinders of 3 mm height, and then the salt was leached out for approximately 30 h in ultrapure water (>18 MOhm/cm) that was replaced regularly. Finally, the scaffolds were coated with poly (vinyl alcohol) (PVA, MW 6000, Polysciences Inc., Chemie Brunschwig, Basel, Switzerland) by immersion into a 1 wt% PVA solution under vacuum. All scaffolds were polarized for 4 h at 6 kV to orient the dipoles of the barium titanate.

Surface Functionalization of Nanocomposite Films and Scaffolds

The surface functionalization with polydopamine (Chien and Tsai, 2013) and arginylglycylaspartic acid (4008998, GRGDS, Bachem, Bubendorf, Switzerland) was established on films and scaffolds. The films were produced by doctor blading the nanocomposite slurry and punching them into 6 mm disks. For non-cell experiments, the films and scaffolds were immersed for 2 and 24 h in a 2 mg/ml dopamine hydrochloride (H8502, Sigma-Aldrich, Merck & Cie, Schaffhausen, Switzerland) in 10 mM, pH 8.5 Tris buffer (T6791, Sigma-Aldrich, Merck & Cie, Schaffhausen, Switzerland). Afterward, they were washed three times with ultrapure water.

Characterization of Functionalized Nanocomposites

The formation of a polydopamine coating through oxidative self-polymerization of dopamine was verified by Raman spectroscopy (inVia, Renishaw, Siebnen, Swizerland) using a 785-nm laser at 500 mW (operated at 10–50% intensity). As a reference, pure polydopamine powder was produced by allowing a 2 mg/ml dopamine hydrochloride solution to self-polymerize in a vacuum oven (Salvislab, Renggli AG, Rotkreuz, Switzerland) at 50 mbar at room temperature. The morphology of polydopamine coating was observed by microscopy (Axio Imager. M2m, Carl Zeiss, Oberkochen, Germany). The water contact angle was measured using a goniometer (OCA 25, DataPhysics Instruments, Filderstadt, Germany) after 3 and 20 s on films and after 1, 3, and 20 s on scaffolds. The droplet volume was 4 µl.

The films and scaffolds that were used for cell experiments were surface functionalized after H_2O_2 plasma sterilization. A 2 mg/ml dopamine solution in Tris buffer and a mixture with 1 mg/ml arginylglycylaspartic acid (RGD, H-1345, Bachem, Bubendorf, Basel) was sterile filtered (0.2 µm, Whatman Puradisc, Merck & Cie, Schaffhausen, Switzerland). The films were covered by pipetting 30 µl of the sterile solution and the scaffolds with 40 µl. Then, the samples were incubated for 2 h in an incubator for 37°C and 5% CO_2 and were afterward washed three times with sterile ultrapure water.

Cell Expansion

The hMSCs (Lonza, Walkersville, United States, male, 19 years old) were isolated from human bone marrow aspirate (Hofmann et al., 2007). The cells were used at passage three and cultured for 7 days under standard cell culture conditions (37°C, 5% CO_2) in expansion medium, composed of Dulbecco's Modified Eagle Medium (DMEM, 41966029 Gibco, Thermo Fisher Scientific, Reinach, Switzerland), 10% fetal bovine serum (FBS, 15240062 Gibco, Thermo Fischer Scientific, Reinach, Switzerland), 1% non-essential amino acids (NEAA, 111140035 Gibco, Thermo Fischer Scientific, Reinach, Switzerland), and 1 ng/ml basic fibroblastic growth factor (bFGF, PHG0369 Gibco, Thermo Fischer Scientific, Reinach, Switzerland), 1% antibiotic-antimycotic (Anti-Anti, 15240062 Gibco, Thermo Fisher Scientific, Reinach, Switzerland) (Hofmann et al., 2007). After trypsinization (0.25%, Gibco, Thermo Fisher Scientific, Reinach, Switzerland), the cells were resuspended in control medium (DMEM, 10% FBS, 1% Anti-Anti) at different concentrations for cell seeding.

Cell Culture on Nanocomposite Films

The nanocomposite films were fixed on standard microscopy glass slides using double-sided polyimide tape (Kapton®, Karl Schupp AG, Zollikerberg, Switzerland) and kept in 35 mm cell culture Petri dishes before H_2O_2 plasma sterilization and surface functionalization. The films were seeded with approximately 6,000 cells by pipetting 30 µl of the cell suspension and allowing them to adhere by 90 min incubation. Afterward, enough control medium was added to fully immerse the glass slide, and the cells were cultured for 1 day to observe cell spreading. Then, the films were washed with phosphate buffered saline (PBS, Medicago, Uppsala, Sweden), fixed using a 4% paraformaldehyde in PBS, incubated for 20 min, and washed again in PBS. The cell-seeded films were permeated by a 0.1% Triton X-100 and 0.5% PBS solution for 5 min and then washed in PBS. F-actin was stained by 90 min incubation in 2 µM phalloidin-TRITC (P1951, Sigma-Aldrich, Merck & Cie, Schaffhausen, Switzerland) in 3% bovine serum albumin (BSA, Sigma-Aldrich, Merck & Cie, Schaffhausen, Switzerland). After washing twice with PBS containing 0.5% BSA, cell nuclei were stained with a 1 µg/ml DAPI (D9542, Sigma-Aldrich, Merck & Cie, Schaffhausen, Switzerland) in PBS solution. All samples were imaged with a Zeiss LSM 780 confocal microscope at 20 × 0.5 NA (Carl Zeiss, Oberkochen, Germany).

Cell Culture on Nanocomposite Scaffolds

The scaffolds were either fixed to polysulfone substrates (2 scaffolds per substrate) and kept in 6 well plates or directly

fixed in 12 well plates using polydimethylsiloxane (10:1 ratio, Sylgard® 184 Elastomer Kit, VWR, Dietikon, Switzerland) (Schädli et al., 2021) or more facile using double-sided 3 M tape (Zhang et al., 2020) before sterilization and surface functionalization. All the scaffolds were seeded with 1.6 Mio cells by pipetting 30 µl of the resuspended cell suspension on top of the scaffold. Then, the scaffolds were incubated for 90 min to allow cell adhesion to the scaffold. Afterward, the cells were cultured in osteogenic medium, which is control medium supplemented with 50 µg/mL L-Ascorbic acid 2-phosphate sesquimagnesium salt hydrate (A8960, Sigma-Aldrich, Merck & Cie, Schaffhausen, Switzerland), 100 nM dexamethasone (D9184, 17 Sigma-Aldrich, Merck & Cie, Schaffhausen, Switzerland), and 10 mM β-glycerophosphate (410990250, Acros Organics, Thermo Fisher Scientific, Reinach Switzerland).

The scaffolds were cultured for 49 days under static conditions directly in 12 well plates using 2 ml osteogenic medium, under static conditions on polysulfone substrates in 6 well plates using 8 ml osteogenic medium, or in dynamic compression bioreactors using 5 ml osteogenic medium. The cell culture medium was replaced three times per week. One of the two scaffolds per bioreactor was loaded with cyclic compression at 5 Hz and 3% strain using an initial preload of 0.2 ± 0.01 N (Schädli et al., 2021). The preload was also used to measure the scaffold's height (Schädli et al., 2021).

Micro-CT Imaging and Processing

High-resolution micro-CT scans were performed on scaffolds that were cultured under static conditions in well plates. The scaffolds were scanned in air before the sterilization. After culturing, the scaffolds were washed with PBS, fixed with 4% paraformaldehyde for 1.5 h at RT, lyophilized overnight (Alpha two to four LDplus, Christ), and then scanned again using a µCT 50 (Scanco Medical). High-resolution scans were obtained from two independent experimental studies with aluminum filter and calibration record and without an aluminum filter. In each experimental study the sample size per group was n = 4 to 6. The energy level was 55 kVp, the current intensity 200 µA, and the integration time 600 ms with a frame averaging of 3, resulting in a resolution of 10 µm. The images were processed using IPL software (V5.42, Scanco Medical, Bassersdorf, Switzerland). After reconstruction, unfiltered scans before culturing were registered on scans after culturing using an intensity-based least-square algorithm (Schulte et al., 2013) adapted with an isotropic scale parameter to account for scaffold shrinkage. Then, the registered images were Gaussian filtered (sigma 1.2, support 1) to reduce noise. Scaffold shrinkage occurred during sterilization with H_2O_2 plasma.

A global threshold was determined for each scaffold composition to account for the different X-ray absorption properties. For each scaffold, a histogram of linear attenuation coefficients was generated using a cylindrical mask with a radius of 2.5 mm and a height of 0.5 mm that lies entirely within the scaffold. Then, a three-parameter lognormal distribution was fitted to the histogram to obtain the density distribution function (Schädli et al., 2021). Note that the histogram was capped at the 90th percentile for the regression because of detector saturation. The threshold was determined as the inflection point after the peak of the distribution, which is the point where the slope of the distribution changes its sign (Carrel et al., 2017). **Supplementary Tables S1–2** list all thresholds determined by this method for the two independent experiments. These image processing steps were done using an in-house developed software framework based on Python 3.6.6 (Python Software Foundation, Delaware) using the SciPy 1.2.0 library (Enthought, Austin, TX).

For image registration of the 3D high-resolution scans, the images were processed as follows using IPL software (V5.42, Scanco Medical, Bassersdorf, Switzerland). The scans from both time-points were thresholded, and structures smaller than 175 voxels were removed by component labeling. This value was used to have a similar volume of voxels removed as in the low-resolution micro-CT (34.5 µm resolution) where typically 50 voxels were removed (Vetsch et al., 2017). Then, the scans taken after the culture were superimposed on images before the culture to obtain a colored image. The colors gray or orange were voxels that were present in both time points or only after the culture, representing the scaffold, mineral formation, and resorption. It should be noted that voxels that were classified as resorption were ignored for the visual analysis as they were caused by registration inaccuracy and scaffold shrinkage, which could only be partially compensated with the isotropic scale parameter.

As the different scaffold compositions influenced the X-ray absorption properties, thus, also influence partial volume effects and beam hardening, modified processing was needed to directly compare the scaffolds with respect to the formed mineral density. The scaffold's mask was created by thresholding the scan from the first time-point at 90% of the determined threshold. Then, the binary image was dilated by one voxel layer. The images from scans after the culture were thresholded at 100% of the determined threshold and then eroded by one voxel layer. Afterward, structures smaller than 175 voxels were removed by component labeling. Using these approaches, the analysis favored mineral formation inside the pores compared to formation sites on the scaffold, avoiding most of the voxels that appear artificially bright (Li et al., 2015).

Time-lapsed micro-CT scans were performed on scaffolds that were cultured in dynamic compression bioreactors (Schädli et al., 2021). Starting from the second week, the scaffolds were scanned weekly in culture medium with a µCT 45 (Scanco Medical, Bassersdorf, Switzerland). The scanning settings were 45 kVp, 177 µA, 600 ms integration without frame averaging, resulting in an isotropic resolution of 34.5 µm after reconstruction. The bioreactors were approximately 40 min outside the incubator for the scan. After reconstruction, the images from follow-up time-points were registered to the scan from Week 2 and Gaussian filtered (sigma 1.2, support 3). A larger support was required to reduce the higher noise from beam hardening at the set resolution.

The image processing was conducted with an in-house software framework based on Python 3.6.6 (Python Software Foundation, Delaware). A cylindrical mask defined the volume of interest in the top 1.0 mm of the scaffold with a 3 mm diameter. Histograms with a bin width of 25 mg HA/cm^3 of the density distributions from Week 2 and Week 7 were plotted for each scaffold using this volume of interest to determine an upper threshold because of a decrease in the number of voxels at high mineral density was observed. The upper threshold was defined where the mineral density distribution from Week 2 intersects with Week 7 (**Supplementary Figure S6**). The upper threshold was calculated as the average of the individual scaffolds and was 1,087 mg HA/cm^3. A mask was generated by thresholding the images with the upper threshold, followed by a one voxel layer dilation. A global threshold was used at 150 HA/cm^3, and unconnected objects smaller than 50 voxels were removed by component labeling to differentiate the mineral from the background. Then, the scaffold mask was applied to the thresholded image. The scaffold mineral density maturation within the volume of interest was calculated for each time-point by normalizing to the scaffold mineral density from the first time-point. The first scan from Week 2 that served as reference for the registration was not included because it was the only scan that was not subject to linear interpolation due to the transformation during image registration. Earlier scanning time-points do not provide a better reference because of an air bubble that vanishes during cell culture (Schädli et al., 2021). The scaffold mineral density maturation rate was calculated by linear fits to the scaffold mineral density maturation as a function of time (Schädli et al., 2021).

Biochemical Assays

The scaffolds (n = 6 per group) were washed twice in PBS after culturing in osteogenic medium. Afterward, the cells were lysed by adding 0.75 ml 0.2% (v/v) Triton X-100 (X100, Sigma-Aldrich, Merck & Cie, Schaffhausen, Switzerland) solution containing 5 mM $MgCl_2$ (208,337, Sigma-Aldrich Merck & Cie, Schaffhausen, Switzerland). The scaffolds were disintegrated with a Mini-Beadbeater (Biospec, Bartlesville, USA) using two steel beads and three rounds at 25,000 rpm for 10 s. Then, the samples were centrifuged at 3,000 x *g*, 5°C for 10 min (Hettich Mikro 200 R, Tuttlingen, Germany). Alkaline phosphatase activity was measured directly afterward using the supernatant. A known amount of five different *p*-nitrophenol (N7660, Sigma-Aldrich, Merck & Cie, Schaffhausen, Switzerland) concentrations in the range of 0–0.5 mmol/l were used as standards. In a 96-well plate, 80 µl of the supernatant was mixed with 20 µl of 0.75 M 2-amino-2-methyl-1-propanol buffer at pH 10.5 (AB113594, abcr GmbH, Karlsruhe, Germany) and 100 µl 10 mM *p*-nitrophenylphosphate solution (71768, Honeywell Fluka™, VWR, Dietikon, Switzerland), and incubated until the developed color was within the standards. The conversion of *p*-nitrophenylphosphate to *p*-nitrophenol was stopped with 0.2 M NaOH. The absorbance values of the samples and standards were measured at 405 nm. The alkaline phosphatase (ALP) activity was calculated using the generated standard curve and normalized with the incubation time and DNA content of the scaffold.

The DNA content was measured using the Quant-iT™ PicoGreen® dsDNA Assay Kit. After the disintegration, the samples were incubated for 48 h at room temperature and then centrifuged at 3,000 x g, 5°C. The assay was conducted following the manufacturer's instructions. A plater reader (Tecan Spark 10 M, Männedorf, Switzerland) was used to measure the fluorescence of the sample supernatant and five standards at an excitation wavelength of 480 nm and a detection wavelength of 520 nm. The DNA amount per scaffold was calculated using the standard curve.

Histology, Immunohistochemistry, and Raman Microscopy Measurements

The scaffolds were fixed in 4% paraformaldehyde for 1.5 h. Vertical or horizontal cryosections of the scaffolds (n = 2) were cut using the Kawamoto method (Kawamoto, 2003) (type 2C, Section-Lab Co. Ltd., Hiroshima, Japan) at a thickness of 10, 16, and 20 µm for histology, Raman microscopy, and immunohistochemistry. The cryosections were glued on microscope slides with a 1 wt% chitosan adhesive. Mineralized extracellular matrix was visualized with von Kossa or Alizarin red staining. The extracellular matrix was stained with hematoxylin and eosin. Collagen was visualized with Sirius Red staining. Brightfield images of the histology sections were taken with a Slide Scanner Panoramic 250 (3D Histech, Budapest, Hungary) at x20. Polarized light micrographs of the sections stained for collagen were taken in transmission mode using a Zeiss AxioImage.Z2 x40 0.9NA. The local Raman spectra were obtained with a 785 nm laser at 500 mW (operated at 10–50% intensity) using an exposure time of 1 min (inVia, Renishaw, Siebnen, Switzerland).

Osteocalcin was imaged by immunofluorescence microscopy. The cryosections were washed three times for 5 min with PBS. Then, the sections were permeabilized with 0.1% Triton X-100 in PBS for 10 min, washed three times with PBS for 5 min and blocked with 3% BSA solution for 1 h, and washed again. Afterward, the cryosections were incubated overnight at 4°C in the dark in anti-osteocalcin (ab93876, abcam) at 1:200 dilution in 1% BSA solution. After the incubation, the samples were rewashed three times for 5 min and incubated for 1 h in the secondary antibody, Alexa Fluor-647 IgG H&L (1:1,000; ab150075, abcam, Cambridge, United Kingdom). The staining was validated with a secondary antibody control without adding the primary antibody and a negative control without any antibody. The stained sections were mounted with fluoroshield (F6182, Sigma-Aldrich, Merck & Cie, Schaffhausen, Switzerland) and imaged using a Leica TCS SP8 setup at x63 1.4 NA (Leica Microsystems, Heerbrugg, Switzerland).

Statistics

The exact sample size is indicated in the figure caption. The data was statistically analyzed using OriginPro 9.6. All the data

are shown as the mean ± s.d. Two-way ANOVA with subsequent Holm-Bonferroni post hoc testing was performed to compare more than two groups and levels. One-way ANOVA with Holm-Bonferroni post hoc testing was conducted for more than two groups. Unpaired and paired Student's t-tests were used to compare two groups. Statistical significance was set at $p < 0.05$.

DATA AVAILABILITY STATEMENT

The raw data supporting the conclusions of this article will be made available by the authors, without undue reservation.

AUTHOR CONTRIBUTIONS

GS, MR, and RM conceived the project. GS and HD conducted surface functionalization experiments. GS, HD, and FC conducted cell experiments. GS and LT conducted micro-CT image analysis. GS, PM, and AL conducted histology and immunohistochemistry experiments. GS wrote the manuscript. RM supervised the project until completion. All authors commented on the manuscript and contributed to its final version.

FUNDING

The research was funded by ETH Zurich. GS has received funding from grant no. ETH-17 15-1.

ACKNOWLEDGMENTS

We highly appreciate Sotiris E. Pratsinis (ETHZ) for his critical comments during project initiation. We thank Dimos Poulikakos (ETHZ) and Thomas Schutzius (ETHZ) for access to the Goniometer, the Scientific Center for Optical and Electron Microscopy (ETHZ) for providing microscopy instrumentation as well as the Central Sterilization Supply Department of USZ. A Python framework to process micro-CT images was made available by Nicholas Ohs (ETHZ). Tanja Minacci (ETHZ) is acknowledged for helping with cell experiments and microscopy work.

SUPPLEMENTARY MATERIAL

The Supplementary Material for this article can be found online at: https://www.frontiersin.org/articles/10.3389/fmats.2021.796044/full#supplementary-material

REFERENCES

Bohner, M., and Miron, R. J. (2019). A Proposed Mechanism for Material-Induced Heterotopic Ossification. *Mater. Today* 22, 132–141. doi:10.1016/j.mattod.2018.10.036

Boonrungsiman, S., Gentleman, E., Carzaniga, R., Evans, N. D., McComb, D. W., Porter, A. E., et al. (2012). The Role of Intracellular Calcium Phosphate in Osteoblast-Mediated Bone Apatite Formation. *Proc. Natl. Acad. Sci.* 109, 14170–14175. doi:10.1073/pnas.1208916109

Bromage, T. G., Goldman, H. M., McFarlin, S. C., Warshaw, J., Boyde, A., and Riggs, C. M. (2003). Circularly Polarized Light Standards for Investigations of Collagen Fiber Orientation in Bone. *Anat. Rec.* 274B, 157–168. doi:10.1002/ar.b.10031

Camarero-Espinosa, S., and Moroni, L. (2021). Janus 3D Printed Dynamic Scaffolds for Nanovibration-Driven Bone Regeneration. *Nat. Commun.* 12, 1031. doi:10.1038/s41467-021-21325-x

Camenzind, A., Schweizer, T., Sztucki, M., and Pratsinis, S. E. (2010). Structure & Strength of Silica-PDMS Nanocomposites. *Polymer* 51, 1796–1804. doi:10.1016/j.polymer.2010.02.030

Carrel, M., Beltran, M. A., Morales, V. L., Derlon, N., Morgenroth, E., Kaufmann, R., et al. (2017). Biofilm Imaging in Porous media by Laboratory X-Ray Tomography: Combining a Non-destructive Contrast Agent with Propagation-Based Phase-Contrast Imaging Tools. *PLoS One* 12, e0180374. doi:10.1371/journal.pone.0180374

Chien, C.-Y., and Tsai, W.-B. (2013). Poly(dopamine)-assisted Immobilization of Arg-Gly-Asp Peptides, Hydroxyapatite, and Bone Morphogenic Protein-2 on Titanium to Improve the Osteogenesis of Bone Marrow Stem Cells. *ACS Appl. Mater. Inter.* 5, 6975–6983. doi:10.1021/am401071f

Damaraju, S. M., Shen, Y., Elele, E., Khusid, B., Eshghinejad, A., Li, J., et al. (2017). Three-dimensional Piezoelectric Fibrous Scaffolds Selectively Promote Mesenchymal Stem Cell Differentiation. *Biomaterials* 149, 51–62. doi:10.1016/j.biomaterials.2017.09.024

Ehterami, A., Kazemi, M., Nazari, B., Saraeian, P., and Azami, M. (2018). Fabrication and Characterization of Highly Porous Barium Titanate Based Scaffold Coated by Gel/HA Nanocomposite with High Piezoelectric Coefficient for Bone Tissue Engineering Applications. *J. Mech. Behav. Biomed. Mater.* 79, 195–202. doi:10.1016/j.jmbbm.2017.12.034

Firoozi, N., and Kang, Y. (2020). Immobilization of FGF on Poly(xylitol Dodecanedioic Acid) Polymer for Tissue Regeneration. *Sci. Rep.* 10, 10419. doi:10.1038/s41598-020-67261-6

Florencio-Silva, R., Sasso, G. R. D. S., Sasso-Cerri, E., Simões, M. J., and Cerri, P. S. (2015). Biology of Bone Tissue: Structure, Function, and Factors that Influence Bone Cells. *Biomed. Res. Int.* 2015, 1–17. doi:10.1155/2015/421746

Gentile, P., Chiono, V., Carmagnola, I., and Hatton, P. (2014). An Overview of Poly(lactic-Co-Glycolic) Acid (PLGA)-based Biomaterials for Bone Tissue Engineering. *Int. J. Mol. Sci.* 15, 3640–3659. doi:10.3390/ijms15033640

Gruber, A. H., Boyer, K. A., Derrick, T. R., and Hamill, J. (2014). Impact Shock Frequency Components and Attenuation in Rearfoot and Forefoot Running. *J. Sport Health Sci.* 3, 113–121. doi:10.1016/j.jshs.2014.03.004

Hagenmüller, H., Hofmann, S., Kohler, T., Merkle, H. P., Kaplan, D. L., Vunjak-Novakovic, G., et al. (2007). Non-invasive Time-Lapsed Monitoring and Quantification of Engineered Bone-like Tissue. *Ann. Biomed. Eng.* 35, 1657–1667. doi:10.1007/s10439-007-9338-2

Hasegawa, T. (2018). Ultrastructure and Biological Function of Matrix Vesicles in Bone Mineralization. *Histochem. Cel Biol.* 149, 289–304. doi:10.1007/s00418-018-1646-0

Hofmann, S., Hagenmüller, H., Koch, A. M., Müller, R., Vunjak-Novakovic, G., Kaplan, D. L., et al. (2007). Control of *In Vitro* Tissue-Engineered Bone-like Structures Using Human Mesenchymal Stem Cells and Porous Silk Scaffolds. *Biomaterials* 28, 1152–1162. doi:10.1016/j.biomaterials.2006.10.019

Kapat, K., Shubhra, Q. T. H., Zhou, M., and Leeuwenburgh, S. (2020). Piezoelectric Nano-Biomaterials for Biomedicine and Tissue Regeneration. *Adv. Funct. Mater.* 30, 1909045. doi:10.1002/adfm.201909045

Kawamoto, T. (2003). Use of a New Adhesive Film for the Preparation of Multi-Purpose Fresh-Frozen Sections from Hard Tissues, Whole-Animals, Insects and Plants. *Arch. Histology Cytol.* 66, 123–143. doi:10.1679/aohc.66.123

Khalid, M., Bora, T., Ghaithi, A. A., Thukral, S., and Dutta, J. (2018). Raman Spectroscopy Detects Changes in Bone Mineral Quality and Collagen Cross-Linkage in Staphylococcus Infected Human Bone. *Sci. Rep.* 8, 9417. doi:10.1038/s41598-018-27752-z

Khare, D., Basu, B., and Dubey, A. K. (2020). Electrical Stimulation and Piezoelectric Biomaterials for Bone Tissue Engineering Applications. *Biomaterials* 258, 120280. doi:10.1016/j.biomaterials.2020.120280

Kitsara, M., Blanquer, A., Murillo, G., Humblot, V., De Bragança Vieira, S., Nogués, C., et al. (2019). Permanently Hydrophilic, Piezoelectric PVDF Nanofibrous Scaffolds Promoting Unaided Electromechanical Stimulation on Osteoblasts. *Nanoscale* 11, 8906–8917. doi:10.1039/C8NR10384D

Ko, E., Yang, K., Shin, J., and Cho, S.-W. (2013). Polydopamine-Assisted Osteoinductive Peptide Immobilization of Polymer Scaffolds for Enhanced Bone Regeneration by Human Adipose-Derived Stem Cells. *Biomacromolecules* 14, 3202–3213. doi:10.1021/bm4008343

Koons, G. L., Diba, M., and Mikos, A. G. (2020). Materials Design for Bone-Tissue Engineering. *Nat. Rev. Mater.* 5, 584–603. doi:10.1038/s41578-020-0204-2

Koroleva, A., Deiwick, A., Nguyen, A., Schlie-Wolter, S., Narayan, R., Timashev, P., et al. (2015). Osteogenic Differentiation of Human Mesenchymal Stem Cells in 3-D Zr-Si Organic-Inorganic Scaffolds Produced by Two-Photon Polymerization Technique. *PLoS One* 10, e0118164. doi:10.1371/journal.pone.0118164

Kozlov, M., Quarmyne, M., Chen, W., and McCarthy, T. J. (2003). Adsorption of Poly(vinyl Alcohol) onto Hydrophobic Substrates. A General Approach for Hydrophilizing and Chemically Activating Surfaces. *Macromolecules* 36, 6054–6059. doi:10.1021/ma021681g

Lee, H., Dellatore, S. M., Miller, W. M., and Messersmith, P. B. (2007). Mussel-Inspired Surface Chemistry for Multifunctional Coatings. *Science* 318, 426–430. doi:10.1126/science.1147241

Li, Z., Kuhn, G., von Salis-Soglio, M., Cooke, S. J., Schirmer, M., Müller, R., et al. (2015). *In Vivo* monitoring of Bone Architecture and Remodeling after Implant Insertion: The Different Responses of Cortical and Trabecular Bone. *Bone* 81, 468–477. doi:10.1016/j.bone.2015.08.017

Liu, W., Li, X., Jiao, Y., Wu, C., Guo, S., Xiao, X., et al. (2020). Biological Effects of a Three-Dimensionally Printed Ti6Al4V Scaffold Coated with Piezoelectric BaTiO3 Nanoparticles on Bone Formation. *ACS Appl. Mater. Inter.* 12, 51885–51903. doi:10.1021/acsami.0c10957

Lopes, H. B., Santos, T. d. S., de Oliveira, F. S., Freitas, G. P., de Almeida, A. L., Gimenes, R., et al. (2013). Poly(vinylidene-trifluoroethylene)/barium Titanate Composite for *In Vivo* Support of Bone Formation. *J. Biomater. Appl.* 29, 104–112. doi:10.1177/0885328213515735

Malhotra, A., Walle, M., Paul, G. R., Kuhn, G. A., and Müller, R. (2021). Application of Subject-specific Adaptive Mechanical Loading for Bone Healing in a Mouse Tail Vertebral Defect. *Sci. Rep.* 11, 1861. doi:10.1038/s41598-021-81132-8

Pobloth, A.-M., Checa, S., Razi, H., Petersen, A., Weaver, J. C., Schmidt-Bleek, K., et al. (2018). Mechanobiologically Optimized 3D Titanium-Mesh Scaffolds Enhance Bone Regeneration in Critical Segmental Defects in Sheep. *Sci. Transl. Med.* 10, eaam8828. doi:10.1126/scitranslmed.aam8828

Schädli, G. N., Büchel, R., and Pratsinis, S. E. (2017). Nanogenerator Power Output: Influence of Particle Size and Crystallinity of BaTiO3. *Nanotechnology* 28, 275705. doi:10.1088/1361-6528/aa75b7

Schädli, G. N., Vetsch, J. R., Baumann, R. P., de Leeuw, A. M., Wehrle, E., Rubert, M., et al. (2021). Time-lapsed Imaging of Nanocomposite Scaffolds Reveals Increased Bone Formation in Dynamic Compression Bioreactors. *Commun. Biol.* 4, 110. doi:10.1038/s42003-020-01635-4

Schemitsch, E. H. (2017). Size Matters: Defining Critical in Bone Defect Size!. *J. Orthop. Trauma* 31, S20–S22. doi:10.1097/BOT.0000000000000978

Scheuren, A. C., Vallaster, P., Kuhn, G. A., Paul, G. R., Malhotra, A., Kameo, Y., et al. (2020). Mechano-Regulation of Trabecular Bone Adaptation Is Controlled by the Local *In Vivo* Environment and Logarithmically Dependent on Loading Frequency. *Front. Bioeng. Biotechnol.* 8, 1–13. doi:10.3389/fbioe.2020.566346

Schipani, R., Nolan, D. R., Lally, C., and Kelly, D. J. (2020). Integrating Finite Element Modelling and 3D Printing to Engineer Biomimetic Polymeric Scaffolds for Tissue Engineering. *Connect. Tissue Res.* 61, 174–189. doi:10.1080/03008207.2019.1656720

Schulte, F. A., Lambers, F. M., Kuhn, G., and Müller, R. (2011). *In Vivo* micro-computed Tomography Allows Direct Three-Dimensional Quantification of Both Bone Formation and Bone Resorption Parameters Using Time-Lapsed Imaging. *Bone* 48, 433–442. doi:10.1016/j.bone.2010.10.007

Schulte, F. A., Ruffoni, D., Lambers, F. M., Christen, D., Webster, D. J., Kuhn, G., et al. (2013). Local Mechanical Stimuli Regulate Bone Formation and Resorption in Mice at the Tissue Level. *PLoS One* 8, e62172. doi:10.1371/journal.pone.0062172

Sundelacruz, S., Moody, A. T., Levin, M., and Kaplan, D. L. (2019). Membrane Potential Depolarization Alters Calcium Flux and Phosphate Signaling during Osteogenic Differentiation of Human Mesenchymal Stem Cells. *Bioelectricity* 1, 56–66. doi:10.1089/bioe.2018.0005

Szewczyk, P. K., Metwally, S., Karbowniczek, J. E., Marzec, M. M., Stodolak-Zych, E., Gruszczyński, A., et al. (2019). Surface-Potential-Controlled Cell Proliferation and Collagen Mineralization on Electrospun Polyvinylidene Fluoride (PVDF) Fiber Scaffolds for Bone Regeneration. *ACS Biomater. Sci. Eng.* 5, 582–593. doi:10.1021/acsbiomaterials.8b01108

Tang, Y., Chen, L., Duan, Z., Zhao, K., and Wu, Z. (2021). Enhanced Compressive Strengths and Induced Cell Growth of 1-3-type BaTiO3/PMMA Bio-Piezoelectric Composites. *Mater. Sci. Eng. C* 120, 111699. doi:10.1016/j.msec.2020.111699

Tang, Y., Wu, C., Wu, Z., Hu, L., Zhang, W., and Zhao, K. (2017). Fabrication and *In Vitro* Biological Properties of Piezoelectric Bioceramics for Bone Regeneration. *Sci. Rep.* 7, 43360. doi:10.1038/srep43360

Vetsch, J. R., Betts, D. C., Müller, R., and Hofmann, S. (2017). Flow Velocity-Driven Differentiation of Human Mesenchymal Stromal Cells in Silk Fibroin Scaffolds: A Combined Experimental and Computational Approach. *PLoS One* 12, e0180781. doi:10.1371/journal.pone.0180781

Washington, M. A., Swiner, D. J., Bell, K. R., Fedorchak, M. V., Little, S. R., and Meyer, T. Y. (2017). The Impact of Monomer Sequence and Stereochemistry on the Swelling and Erosion of Biodegradable Poly(lactic-Co-Glycolic Acid) Matrices. *Biomaterials* 117, 66–76. doi:10.1016/j.biomaterials.2016.11.037

Yang, Z., Liu, M., Yang, Y., Zheng, M., Yang, Y., Liu, X., et al. (2020). Biofunctionalization of Zirconia with Cell-Adhesion Peptides via Polydopamine Crosslinking for Soft Tissue Engineering: Effects on the Biological Behaviors of Human Gingival Fibroblasts and Oral Bacteria. *RSC Adv.* 10, 6200–6212. doi:10.1039/C9RA08575K

Zhang, C., Liu, W., Cao, C., Zhang, F., Tang, Q., Ma, S., et al. (2018). Modulating Surface Potential by Controlling the β Phase Content in Poly(vinylidene Fluoridetrifluoroethylene) Membranes Enhances Bone Regeneration. *Adv. Healthc. Mater.* 7, 1701466. doi:10.1002/adhm.201701466

Zhang, C., Wang, W., Hao, X., Peng, Y., Zheng, Y., Liu, J., et al. (2021). A Novel Approach to Enhance Bone Regeneration by Controlling the Polarity of GaN/AlGaN Heterostructures. *Adv. Funct. Mater.* 31, 2007487. doi:10.1002/adfm.202007487

Zhang, J., Wehrle, E., Adamek, P., Paul, G. R., Qin, X.-H., Rubert, M., et al. (2020). Optimization of Mechanical Stiffness and Cell Density of 3D Bioprinted Cell-Laden Scaffolds Improves Extracellular Matrix Mineralization and Cellular Organization for Bone Tissue Engineering. *Acta Biomater.* 114, 307–322. doi:10.1016/j.actbio.2020.07.016

Zhang, X., Zhang, C., Lin, Y., Hu, P., Shen, Y., Wang, K., et al. (2016). Nanocomposite Membranes Enhance Bone Regeneration through Restoring Physiological Electric Microenvironment. *ACS Nano* 10, 7279–7286. doi:10.1021/acsnano.6b02247

Zhang, Y., Chen, L., Zeng, J., Zhou, K., and Zhang, D. (2014). Aligned Porous Barium Titanate/hydroxyapatite Composites with High Piezoelectric Coefficients for Bone Tissue Engineering. *Mater. Sci. Eng. C* 39, 143–149. doi:10.1016/j.msec.2014.02.022

Conflict of Interest: The authors declare that the research was conducted in the absence of any commercial or financial relationships that could be construed as a potential conflict of interest.

Publisher's Note: All claims expressed in this article are solely those of the authors and do not necessarily represent those of their affiliated organizations, or those of the publisher, the editors, and the reviewers. Any product that may be evaluated in this article, or claim that may be made by its manufacturer, is not guaranteed or endorsed by the publisher.